Available online at www.sciencedirect.com
ScienceDirect
Journal of Nuclear Materials 374 (2008) 138–146
journal of nuclear materials
www.elsevier.com/locate/jnucmat

Examination of residual stresses and texture in zirconium alloy cladding tubes after a large plastic deformation: Experimental and numerical study

D. Gloaguen *, T. Berchi, E. Girard, R. Guillén

GeM, Institut de Recherche en Génie Civil et Mécanique, Université de Nantes, Ecole Centrale de Nantes, CNRS UMR 6183, 37 Boulevard de l'Université, BP 406, 44 602 Saint-Nazaire, France

Received 11 May 2007; accepted 25 July 2007

Abstract

X-ray diffraction is used to assess the development of residual stresses within the grains of Zr alloy tubes processed via cold pilgering. A modified elastoplastic self-consistent model was used to simulate the texture and the internal stresses developments. The influence and the role of elastoplastic anisotropy were also studied and explained in this work. The contribution and the magnitude of the first- as well as the second-order residual stresses were correctly evaluated using information from the model. Comparison between the X-ray diffraction results (texture *and* residual strains) and the simulations confirms that prismatic slip is the main active deformation mode in this alloy under large strain.

PACS: 46.35.+z; 61.10.Nz; 62.20.Fe; 81.05.Bx; 83.60.−a

1. Introduction

Zirconium alloys are extensively used in various types of fission reactors. The development of zirconium alloys is essentially due to the nuclear industry, where zirconium alloys have been regarded as the proven structural material [1]. In this work, we are concerned by the manufacturing process of M5™ alloy cladding tubes by cold pilgering. This process is a tube forming operation where the inner radius and wall thickness are both progressively reduced between a fixed axisymmetric mandrel and forward- and backward-rolling grooved dies [2]. This process consists in a sequence of three rolling passes. After each pass, the tube is heat treated at a certain annealing temperature, which is sufficient to induce recrystallization, except for the last heat treatment, which is done just for stress relieving.

Zr alloys have a hcp crystal structure and exhibit high anisotropic plastic properties at mesoscopic (grain) and macroscopic levels with various active deformation modes. These properties and the crystallographic texture explain the appearance and development of important residual stresses when an elastoplastic deformation is introduced. These stresses are termed intergranular or second-order stresses. They depend on initial and induced crystallographic textures. The engineering consequences of second-order stresses with strong texture may be severe. The texture and stresses at a given step in the fabrication process will influence the formability with which the next mechanical process might be realised. The texture of the material will have a significant effect on its in-service performance because irradiation creep, yield strength, stress corrosion cracking resistance, for example, are strong functions of texture. During the process, internal stresses can also induce defects such as transverse cracks or surface damage [1,3].

* Corresponding author.
E-mail address: david.gloaguen@univ-nantes.fr (D. Gloaguen).

0022-3115/$ - see front matter © 2007 Elsevier B.V. All rights reserved.
doi:10.1016/j.jnucmat.2007.07.017

Therefore, metal forming processes optimization such as rolling requires knowledge of the evolution of the material's anisotropic elastoplastic behaviour during the deformation operations. Polycrystal models for numerical prediction of deformation processes have undergone an important development during the last years. The modelling of the plastic deformation of metallic polycrystals can be carried out by deductive methods based on strain mechanisms and scale transition methods like self-consistent (SC) models [4–6]. Polycrystal models are typically evaluated by their ability to simulate the mechanical behaviour. For large deformations (>20% strain), model predictions are readily compared to textures determined experimentally by X-ray or neutron diffraction.

Hexagonal materials are characterised by a wide variety of possible deformation systems. It is necessary to know both the texture and the deformation mechanisms to be able to model these mechanical properties. This requires, in particular, a proper knowledge of the deformation mechanisms with their corresponding CRSS (critical resolved shear stresses). Only few data are available for CRSS in the literature. Moreover, the CRSS generally depend significantly on the contents of alloying elements. In spite of this very basic knowledge of these data, many authors have tried to model the mechanical properties of hexagonal materials after large deformation. In these cases, the approach consists in finding the set of material parameters offering the best agreement with crystallographic texture by applying a polycrystalline model. Realistic simulations of deformation texture development of Zr alloys can be done using the viscoplastic SC model [7–9]. The cold pilgering texture of zirconium alloy has been also studied with this kind of approach [3,10]. The confrontation between simulations and experimental texture shows that the prismatic slip is probably the most active system for this process.

In the present work, a different approach is proposed to validate the accuracy and the relevance of theoretical model for hexagonal material in a large deformation framework. *Both texture and residual stresses* characterisation by diffraction have been used simultaneously to evaluate polycrystal models for non-cubic material. A confrontation between experimental observations (X-ray diffraction) and predictions of an elastoplastic self-consistent (EPSC) model has been made in order to obtain more information about the different factors responsible for the appearance of residual second-order stresses and determine with more accuracy the set of deformation systems. This comparison allows a better understanding and interpretation of diffraction and mechanical results.

The aim of the present study is the analysis and understanding of the anisotropic elastoplastic behaviour evolution during the cold pilgering operation of zirconium alloy. A modified EPSC model was used to predict the behaviour of zirconium alloy cladding tubes during the last rolling pass. This approach is well suited to study anisotropic materials with multiple slip and twinning modes because it allows for different deformation depending on the relative orientation between the grain and the average medium. X-ray diffraction results (texture and residual stresses) obtained at the initial and final states provide an accurate experimental base for determining the appropriate model parameters and find a realistic combination of deformation systems. The theoretical stresses are compared with the experimental results obtained by X-ray diffraction. The results predicted by the SC model are discussed. In hexagonal alloys, like those of zirconium, plastic anisotropy induces plastic incompatibility stresses. These intergranular plastic stresses must be taken into account for a proper interpretation of X-ray experimental data. Consequently, a specific study concerning the influence of these second-order stresses, as well as the first-order (macroscopic) stresses, has also been performed.

2. Experimental procedure

The analysis was performed for the last cold pilgering pass. In this work, we analysed the texture and residual stresses in two states: before and after the third pass cold work. At the initial state, tubes have been submitted to a recrystallization treatment at 700 °C. At the initial state, the dimensions of M5™ tubes are: 17.8 mm external diameter and 2 mm thickness. The dimensions after forming (195% total strain) are 8.37 mm and 0.6 mm. The chemical composition is (Wt%-balance = Zr): Nb(1.0), Fe(0.035) and O(0.13).

2.1. Texture analysis

X-ray diffraction analysis was performed with four circles XRD3003PTS SEIFERT goniometer. Kα copper radiation was used. The X-ray beam output collimator had 0.5 mm diameter. The diffraction peaks were recorded with a position sensitive detector (PSD). We measured incomplete pole figures (PF) on a $5 \times 5°$ grid with tilt and azimuth angles ranging from 0° to 60° and 0° to 360°, respectively. For each experimental direction, the diffraction pattern was adjusted, using a nonlinear least squares analysis and assuming pseudo-Voigt peak profiles for each peak, to evaluate background noise and to obtain peak intensities. The study of samples having a curved geometry not only requires an accurate positioning of the samples but also take into account the geometric effects induced by XRD directional feature. A theoretical model based on a ray-tracing method was used to take into account the geometric effects, which modify the collected intensities. More details of this approach can be found in [11]. Correction coefficients accounting for the 'geometrical texture' of the samples as well as absorption corrections are calculated. The obtained results are used to correct experimental pole figures. The orientation distribution function (ODF) calculation has been performed with experimental PF $\{0002\}$, $\{10\bar{1}1\}$, $\{11\bar{2}0\}$ and $\{10\bar{1}3\}$ with help of WIMV algorithm implemented in the BEARTEX program package [12].

2.2. Residual stresses

We present succinctly the principles of residual stresses determination by X-ray diffraction and the key role played by elastic and plastic anisotropy properties on the interpretation of the data. More details can be found in Refs. [13–17].

Residual stresses are generated by inhomogeneous plastic deformation on two scales: one length scale is given by the size of the component, the second by the size of the grain forming the polycrystalline aggregate. The inhomogeneity on the sample length scale gives the macroscopic stress field or first-order stress, while the inhomogeneity on the grain size scale gives the intergranular or second-order stress. Both are superimposed, and X-ray diffraction measurements give a combination of first- and second-order stresses. In order to determine first-order residual stresses, intergranular stresses must thus be subtracted from the given stress field. The important question is how to obtain the macroscopic strain from the measured strain in a hexagonal component observed with the aid of a specific $\{hkil\}$ plane when we have a superposition of both macroscopic and important intergranular contributions. In the present work, the method proposed by Baczmanski et al. [13] for cubic material is used and extended to hexagonal material.

For a direction of the scattering vector defined by the angles ϕ and ψ, the measured strain can be expressed by

$$\langle \varepsilon(\phi,\psi,hkil)\rangle_{V_d} = F_{ij}(\phi,\psi,hkil)\sigma^{I}_{ij} + \langle \varepsilon^{IIpi}(\phi,\psi,hkil)\rangle_{V_d}. \quad (1)$$

$F_{ij}(\phi,\psi,hkil)$ are the diffraction elastic constants for the $\{hkil\}$ reflection and $< >_{V_d}$ is the average over diffracting grains for the $\{hkil\}$ reflection. $\langle \varepsilon^{IIpi}(\phi,\psi,hkil)\rangle_{V_d}$ ('pi' means plastic incompatibility) is the elastic strain caused by plastic incompatibilities of grains. σ^{I} denotes the macroscopic stress tensor.

The relation (1) shows clearly that the measured strain cannot be identified to the macroscopic strain if the material presents plastic anisotropic properties. The presence of intergranular strain after a mechanical solicitation influences the measured strain. Generally, the interpretation of experimental data is based on the unjustified assumption that $\langle \varepsilon^{IIpi}(\phi,\psi,hkil)\rangle_{V_d} = 0$. In our study, we propose to quantify the importance of these intergranular stresses and to show their influence in the interpretation of the experimental results.

With the Baczmanski's method, some information obtained from the scale transition method are used. The mesoscopic residual stresses after the rolling process for each grain can be predicted. So, the average $\langle \varepsilon^{IIth}(\phi,\psi,hkil)\rangle_{V_d}$ ('th' means theoretical model) strain for diffracting grains volume can be calculated. The second term in Eq. (1) is assumed to be approximated by

$$\langle \varepsilon^{IIpi}(\phi,\psi,hkil)\rangle_{V_d} = q\langle \varepsilon^{IIth}(\phi,\psi,hkil)\rangle_{V_d}. \quad (2)$$

q is a constant factor. It is introduced in order to find the real magnitude of elastic strains of plastic origin assuming that their variation with ψ and ϕ angles is correctly described by the model. Using a EPSC model, we predict values of the residual stresses for every crystalline orientation and we calculate the average $\langle \varepsilon^{IIth}(\phi,\psi,hkil)\rangle_{V_d}$ strain for the diffracting volume.

For known $F_{ij}(\phi,\psi,hkil)$, theoretically predicted strain $\langle \varepsilon^{IIth}(\phi,\psi,hkil)\rangle_{V_d}$ and measured deformations $\langle \varepsilon^{IIth}(\phi,\psi,hkil)\rangle_{V_d}$, the other quantities from the Eq. (1) (the unknowns are q and the first-order stress) can be determined using a nonlinear fitting procedure to give a complete description of the stress (and strain) field in a plastically deformed polycrystalline material.

We have determined the evolution of internal stresses due to plastic anisotropy in the deformed sample after rolling test. These experiments were carried out on a XRD3003PTS SEIFERT goniometer with $Cr K_\alpha$ and $Cu K_\alpha$ radiations. An Ω goniometric assembly with a position sensitive detector were used. Three plane families were studied with Cr radiation: $\{10\bar{1}4\}$ at $2\theta = 156.7°$, $\{20\bar{2}2\}$ at $2\theta = 137.2°$ and $\{0004\}$ at $2\theta = 125.6°$. With Cu radiation, the three plane analysed were: $\{20\bar{2}5\}$ at $2\theta = 136.8°$, $\{30\bar{3}2\}$ at $2\theta = 123.0°$ and $\{21\bar{3}3\}$ at $2\theta = 117.8°$. Fig. 1 shows the (hkl) plane normal orientation in a basal stereographic projection of the hexagonal lattice. Diffractograms were recorded for sixteen tilt angles ψ varying between $-48°$ and $+45°$ and for one azimuthal angle $\phi = 0°$. The direction $\phi = 0°$ corresponds to the rolling direction. The X-ray beam output collimator had a 0.5 mm diameter. The errors due to geometry effects is weak with the X-ray beam diameter used [18]. The set of diffraction peaks obtained for all the tilt angles was fitted simultaneously with a pseudo-Voigt function, which took into account the $K_{\alpha1}$–$K_{\alpha2}$ contribution. The centroid of the fitted diffraction line was taken as the peak position. For each diffraction peak, the background was fitted by a polynomial function. The diffraction elastic constants $F_{ij}(\phi,\psi,hkil)$

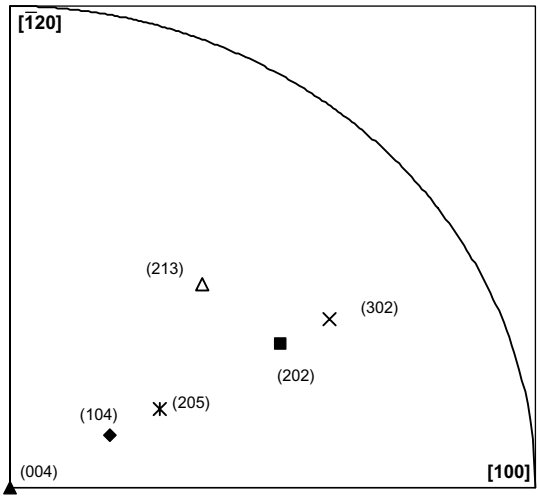

Fig. 1. (hkl) plane normal orientation in a basal stereographic projection of the hexagonal lattice.

are theoretically calculated with an elastic SC model. The influence of the texture on these constants is taken into account by weighting single crystal elastic constants with the texture function (1000 grains). According to Ref. [15], the $F_{ij}(\phi,\psi,hkil)$ are defined as

$$F_{ij}(\phi,\psi,hkil)=\frac{\partial\langle\varepsilon(\phi,\psi,hkil)\rangle_{V_d}}{\partial\sigma^{I}_{ij}}. \tag{3}$$

They connect the strain determinable by diffraction methods to the stress σ^{I} within a textured sample. For their calculation, the strains in the measuring direction m have to be averaged considering the crystals with the $\{hkil\}$ normal parallel to the direction m (described by the angles (ϕ,ψ)) and being rotated by any angle α about it.

$$F_{ij}(\phi,\psi,hkil)=\frac{\int_0^{2\pi}\frac{\partial\varepsilon^{II}_{kl}(\Omega)}{\partial\sigma^{I}_{ij}}f(\Omega)m_k m_l\mathrm{d}\alpha}{\int_0^{2\pi}f(\Omega)\mathrm{d}\alpha} \tag{4}$$

$\varepsilon^{II}(\Omega)$ is the mesoscopic strain tensor of each contributing crystal defined by an orientation Ω. $f(\Omega)$ denotes the orientation distribution function of the crystallites (the experimental texture of the final tube is used in the paper).

At this point, a model assumption about the dependence of the crystal strains on the stress σ^{I} is required:

$$\frac{\partial\varepsilon^{II}_{kl}(\Omega)}{\partial\sigma^{I}_{ij}}=A(\Omega), \tag{5}$$

with

$$\varepsilon^{II}(\Omega)=A(\Omega)..\sigma^{I}. \tag{6}$$

$A(\Omega)$ is determined by the elastic self-consistent model (Kröner–Eshelby model). Only the experimental ODF is required to determine the F_{ij}.

After that, a stress tensor $\sigma^{exp}_{ij}(hkil)$ is calculated by the following relation:

$$\langle\varepsilon(\phi,\psi,hkil)\rangle_{V_d}=F_{ij}(\phi,\psi,hkil)\sigma^{exp}_{ij}(hkil). \tag{7}$$

These experimental stresses vary with the $\{hkil\}$ reflection due to the plastic anisotropy. In this case, the second-order stresses of plastic origin $\langle\varepsilon^{IIpi}(\phi,\psi,hkil)\rangle_{V_d}$ in relation (1) is supposed to be equal to 0. In a second step, the complete relation (1) is used with an EPSC model to determine both the first- as well as the second-order stresses.

3. Self-consistent modelling

The principles for using the SC model to predict elastoplastic deformation were proposed by Kröner and Hill [19,20]. In the present work, the model developed in Ref. [4] is used. For a more detailed description of the EPSC model, see Refs. [21,22]. Each grain is assumed to have the form of an ellipsoidal inclusion in a homogeneous effective medium (HEM) whose properties are the average of all the other grains in the assembly. The polycrystal is represented by a weighted discrete distribution (1000 grains) of orientations (Euler angles $(\varphi_1\phi\varphi_2)$). Lattice rotation (reorientation by slip and twinning) and texture changes are incorporated in the model. For the sake of clarity, the small strain formulation is used for the model presentation.

The principal modification, which is rapidly discussed here, concerns the selection of active slip systems. The new algorithm is much faster and resolves the problem of the ambiguous selection of slip systems. The plastic flow can take place in a grain when the Schmid criterion is verified, i.e. slip (or twinning) occurs if the resolved shear stress τ^{g} on a system g is equal to the critical value τ^{g}_{c} depending on the hardening state of the slip system. This necessary condition is insufficient, and the complementary condition, which states that the increment of the resolved shear stress must be equal to the incremental rate of the CRSS, has to be checked simultaneously. The resolved shear stress is defined as the projection of the mesoscopic stress tensor σ^{II} on the considered deformation system. In small strain formulation, one has:

$$\tau^{g}=R^{g}..\sigma^{II}=\tau^{g}_{c}\quad\text{and}\quad\dot{\tau}^{g}=R^{g}..\dot{\sigma}^{II}=\dot{\tau}^{g}_{c}, \tag{8}$$

where R^{g} is the Schmid tensor on a system g. $A..B$ denotes the double scalar product $A_{ijkl}B_{klmn}$ using the Einstein summation convention.

The main problem is to determine which combination of slip systems will actually be activated at each step of the plastic deformation path. In this case, all possible combinations of potentially active systems must be scanned to find one that satisfies the two previous conditions (Eq. (8)) simultaneously. Because this must be done in a large deformation framework, running time considerations become one of the main problems of the model. Moreover, this method can give several equivalent solutions for some hardening matrices [23]. Recently, Ben Zineb et al. [24] have proposed a new formulation. This one was extended to the polycrystalline model framework by Lorrain et al. [25]. The accuracy of the simulations was also evaluated at the meso- and macroscopic levels by referring to mechanical experiments (tensile tests, neutron diffraction) [26]. It should be noticed that the 'classic' EPSC model and the modified one give similar results: the main active systems, predicted texture and residual strains are similar. Based on the work of Ben Zineb et al., the slip rate on a system g can be expressed with the following equation:

$$\dot{\gamma}^{g}=M^{g}\left(\tau^{g},\tau^{g}_{c}\right)\dot{\tau}^{g}. \tag{9}$$

The slip rate is linked to the resolved shear stress rate through a function M^{g}.

The hardening parameter M^{g} is given by [24]:

$$M^{g}=\frac{1}{H^{gg}}\left[\frac{1}{2}\left(1+\mathrm{th}\left(k_0\left(\frac{\tau^{g}}{\tau^{g}_{c}}-1\right)\right)\right)\right]\left[\frac{1}{2}(1+\mathrm{th}(k_1\dot{\tau}^{g}))\right]\times\left[\frac{1}{2}(1+\mathrm{th}(k_2\tau^{g}))\right], \tag{10}$$

where k_0, k_1 and k_2 are numerical parameters. H^{gg} is the self-hardening parameter defined in Eq. (12). The Hyperbolic tangent function was tested and used because it per-

mits to reproduce the mechanical and hardening behaviours. The slip rate can be written as

$$\dot{\gamma}^g = M^g \dot{\tau}^g = M^g R^g .. \dot{\sigma}^{\mathrm{II}} \quad \text{(without summation over } g\text{)}. \tag{11}$$

If an additive decomposition of strain rate $\dot{\varepsilon}^{\mathrm{II}}$ on elastic and plastic parts is used:

$$\dot{\varepsilon}^{\mathrm{II}} = \dot{\varepsilon}^{\mathrm{IIe}} + \dot{\varepsilon}^{\mathrm{IIp}}. \tag{12}$$

By using the usual generalized Hooke's law and Eq. (11), the slip rate on a system g becomes:

$$\dot{\gamma}^g = M^g R^g .. (c .. \dot{\varepsilon}^{\mathrm{IIe}}). \tag{13}$$

The plastic strain rate $\dot{\varepsilon}^{\mathrm{IIp}}$ is related to the tensor R^g and the slip rate $\dot{\gamma}^g$ in the system g by the expression:

$$\dot{\varepsilon}^p = \sum_g R^g \dot{\gamma}^g. \tag{14}$$

With Eqs. (12)–(14), one obtains, after calculations, the following relation:

$$\dot{\gamma}^g = \sum_h \left(\delta_{gh} + M^g R^g .. c .. R^h\right)^{-1} .. M^h R^h .. c .. \dot{\varepsilon}^{\mathrm{II}}. \tag{15}$$

It is usual to introduce a hardening matrix H^{gh} to describe the evolution of CRSS rate in a system g as a function of the plastic slip (or twinning) on the other systems:

$$\dot{\tau}_{\mathrm{c}}^g = \sum_h H^{gh} \dot{\gamma}^h. \tag{16}$$

With relations (8), (11) and (12) and the usual generalized Hooke's law, the constitutive elastoplastic relationship for the single crystal can be deduced:

$$\dot{\sigma}^{\mathrm{II}} = \left[c - \sum_g \sum_h c .. R^g \left(\delta_{gh} + M^g R^g .. c(\Omega) .. R^h\right)^{-1} M^h R^h .. c \right] .. \dot{\varepsilon}^{\mathrm{I}} = \ell .. \dot{\varepsilon}^{\mathrm{II}}, \tag{17}$$

where ℓ is the tensor of tangent elastoplastic moduli of the single crystal.

The relation between the stress rate $\dot{\sigma}^{\mathrm{I}}$ and the strain rate $\dot{\varepsilon}^{\mathrm{I}}$ can be written for the macro-scale as follows:

$$\dot{\sigma}^{\mathrm{I}} = L .. \dot{\varepsilon}^{I}, \tag{18}$$

where L is the macroscopic tangent modulus for the fictional average homogeneous medium. The local strain and stress rates can be obtained classically through the localization A and concentration B tensors:

$$\dot{\varepsilon}^{\mathrm{II}} = \left(\mathrm{I} + S^{\mathrm{esh}} .. L^{-1} .. \Delta\ell\right)^{-1} .. \dot{\varepsilon}^{\mathrm{I}} = A .. \dot{\varepsilon}^{\mathrm{I}}, \tag{19}$$

$$\dot{\sigma}^{\mathrm{II}} = \ell .. \left(\mathrm{I} + S^{\mathrm{esh}} .. L^{-1} .. \Delta\ell\right)^{-1} .. L^{-1} .. \dot{\sigma}^{\mathrm{I}} = \ell .. A .. L^{-1} .. \dot{\sigma}^{\mathrm{I}} = B .. \dot{\sigma}^{\mathrm{I}}, \tag{20}$$

where $\Delta\ell = \ell - L$. S^{esh} is the Eshelby tensor.

The volume averages of the local stress and strain tensors must coincide with the overall strain and stress. After some algebraic calculations, these conditions give the overall elastoplastic tensor L as a weighted average of the mesoscopic tensor ℓ:

$$L = \left\langle \ell .. \left[I + S^{\mathrm{esh}} .. L^{-1} .. \Delta\ell \right]^{-1} \right\rangle. \tag{21}$$

Eq. (21) is a nonlinear implicit equation because S^{esh} depends on the unknown L in the framework of EPSC theory. The Eshelby tensor is calculated by an integral equation [21] that takes the plastic anisotropy fully into account. This equation is solved iteratively. Once L is known, by specifying an overall stress or strain increment, the model can give the corresponding stress or strain tensors for each orientation. Therefore, the mechanical response of the polycrystal can be described.

3.1. Data used in the simulations

For hexagonal materials, like zirconium, because of the relatively strong crystallographic anisotropy, several modes may be active: slip and/or twinning systems. In such materials, prismatic glide $\{10\bar{1}0\}\langle 11\bar{2}0\rangle$ is reported to be the main active deformation mode [27,28]. First-order pyramidal slips $\{10\bar{1}1\}\langle 11\bar{2}3\rangle$ and $\{10\bar{1}1\}\langle 11\bar{2}0\rangle$ are generally presented as secondary slip modes [28,29]. At room temperature, twinning has also been observed in zirconium samples [30,31]. Twinning of $\{10\bar{1}2\}$ and $\{11\bar{2}1\}$ types is expected in extension along the $\vec{c}$ axis whereas twinning of $\{11\bar{2}2\}$ and $\{10\bar{1}1\}$ types is expected in compression along the $\vec{c}$ axis.

The initial CRSS are taken as identical for all systems of a system type. The deformation systems introduced in the model are assumed to be: prismatic slip denote pr$\langle a\rangle$, first-order pyramidal slip (pyr$\langle c+a\rangle$ and pyr$\langle a\rangle$) and $\{10\bar{1}2\}$ twinning (ttw).

Different authors [3,10] have shown that a good qualitative agreement with the experimental textures and the deformation systems activity for cold-rolled Zr alloys can be obtained selecting pr$\langle a\rangle$, pyr$\langle c+a\rangle$, ttw and/or ctw (compressive twinning) as active deformation modes. Basal slip is not included in the set of deformation modes because some discrepancies appear with the X-ray results if this slip system is an active deformation mode.

In this work, we consider a linear hardening law [4] where the coefficient H^{gr} is equal to H^{gg} for any deformation modes r: $\dot{\tau}^g = H^g \sum_r \dot{\gamma}^r$, that is, latent hardening is equal to the self-hardening. In the model, CRSS and the hardening law for slip and twinning are considered as controlling parameters. Their values depend on many factors (oxygen content, grain size, temperature...) [32] and are unknown. Contrary to previous works [3,10], the approach used in this study consists in finding the set of material parameters offering the best agreement with crystallographic texture and residual stresses by applying the EPSC model. In a first step, the effect of deformation modes on the predicted strain (and stress) and texture was systematically analysed. Each deformation mode was applied within the EPSC model independently, in

Table 1
Material parameters used in the simulations

$\tau^{pr\langle a\rangle}$ (MPa)	$\tau^{pyr\langle a\rangle}$ (MPa)	$\tau^{pyr\langle c+a\rangle}$ (MPa)	τ^{ttw} (MPa)
95	175	310	180
$H^{pr\langle a\rangle}$ (MPa)	$H^{pyr\langle a\rangle}$ (MPa)	$H^{pyr\langle c+a\rangle}$ (MPa)	H^{ttw} (MPa)
80	170	200	180
k_0	k_1	k_2	β (MPa^{-1})
25	1	1	$1/H^{rr}$

order to examine its effect on the strain accumulation and the texture. The effect of combining two or three systems was also examined. The value and the sign of the predicted strains were much more different than those detected experimentally. The observed trends and magnitude of texture and strains were not reproduced correctly by the model in the case of one or two deformation mode. Finally, all the four deformation systems were applied simultaneously with different set of material parameters (CRSS, hardening matrix). The best agreement was found with the values given in Table 1. A comparison with experimental texture and stresses constitutes an accurate and relevant validation of the choice of deformation systems. It is a good way of evaluating the overall agreement between the model and the experiment. For example, it is possible to explain and reproduce the texture without the pyr$\langle a\rangle$ system. However the model cannot simulate correctly experimental residual stresses. Only the four systems with pr$\langle a\rangle$ as the main deformation mode can explain each experimental result. The comparison between stress and texture obtained with X-ray diffraction measurements on these samples and simulations is presented in the fifth part.

4. X-ray diffraction results

Initial textures are shown in Fig. 2, where 'RD' denotes the rolling direction, 'TD' the transverse direction and 'ND' the normal one. It can be noticed that the initial tube presents an asymmetry in the ND–TD plane despite a chemical layer removal (50 μm). This phenomenon is not linked to the friction due to the mechanical sollicitation. The texture of the undeformed sample is probably due to a recrystallization during the thermal treatment. The prismatic PF exhibits intensity maxima along the RD.

Fig. 2 also shows the PF after the mechanical tests. A 'classic' texture evolution is observed for the prismatic and basal PF [28]. In the final state, the {0002} PF shows a bimodal distribution of the intensity maxima in the NT–TD plane at about 30° of the ND axis. This is typical for this kind of sample.

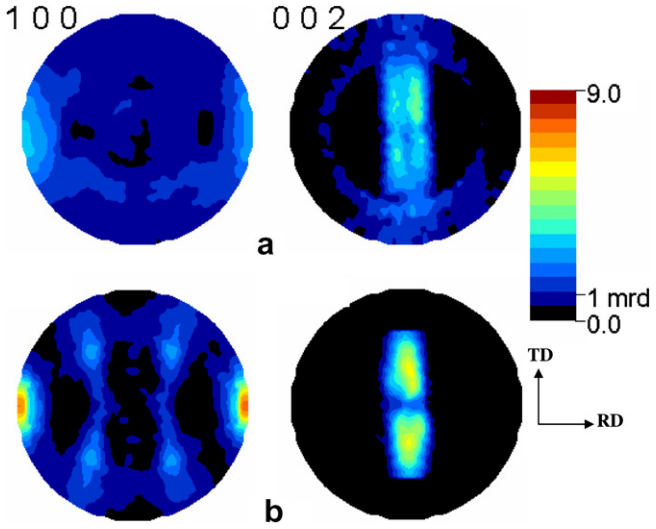

Fig. 2. Initial (a) and final (b) {0002} and {10$\bar{1}$0} PF.

The longitudinal stress $\sigma_{11}^{exp}(hkil)$ ($\phi = 0°$) was terminated with the relation (7). The residual stresses on the undeformed sample are weak: -22 ± 17 MPa for the {0004} plane, $+23 \pm 6$ MPa for the {20$\bar{2}$2} plane and $+73 \pm 3$ MPa for the {20$\bar{2}$5} plane. These results show that the initial mechanical state is relatively homogenous within the sample and the thermal residual stresses are negligible. Table 2 shows the experimental results obtained with X-ray diffraction at 195% strain. The stress values vary strongly from one plane to another. For example, $\sigma_{11}^{exp}(hkil)$ value reaches $+189 \pm 16$ MPa for {10$\bar{1}$4} and -376 ± 14 MPa for {30$\bar{3}$2}. X-ray measurements show the effective existence of plastic anisotropy. As can be seen from Eq. (1), the measured stress depends on a function of the analysed plane family. Strain incompatibilities are present at the mesoscopic level in the material; consequently, the stresses obtained by X-ray diffraction depend on the plane. The diffracting crystals are not the same for each case and this allows us to deduce that different second-order stresses exist, linked to a strong plastic anisotropic deformation for these plane families. With the help of FDO, it is possible to find the set of principal orientations, which contribute to the diffracting volume for the different ψ values (between $-48°$ and $+45°$) and for each plane. For example, because of the final texture, most of the {10$\bar{1}$4} planes have the $\vec{c}$ axis making an angle between 0° and 25° with the sample surface whereas this axis is located preferentially between 25° and 80° in relation to the surface for the {30$\bar{3}$2} planes. Because of second-order stresses, the obtained values are not directly related to those obtained by macroscopic methods [33].

Table 2
Experimental longitudinal stress $\sigma_{11}^{exp}(hkil)$ obtained with different crystallographic planes

Plane	{21$\bar{3}$3}	{30$\bar{3}$2}	{0004}	{20$\bar{2}$2}	{20$\bar{2}$5}	{10$\bar{1}$4}
Stress (MPa)	-334 ± 6	-376 ± 14	-185 ± 39	-226 ± 24	-174 ± 19	$+189 \pm 16$

Errors values were determined from the standard deviations of the peak positions as obtained from peak fitting.

5. Simulations results and discussion

The EPSC model is used to simulate the residual intergranular strains (or stresses) and crystallographic texture after loading along the RD. The mesoscopic stresses are then averaged and projected on the $\phi\psi$ directions to simulate the diffracting volume behaviour, and the simulated crystallographic reorientation is also obtained.

The predicted PF for the final tube are given in Fig. 3. As shown in this figure, there is an agreement between the experiment results and the EPSC model. The principal features of experimental texture are reproduced by the simulations. We clearly see the predicted basal poles that are, preferentially oriented at 38° from RD in the RD–TD plane. With the CRSS values chosen above, deformation is accommodated through pr$\langle a\rangle$ and pyr$\langle c+a\rangle$. As can be seen in Fig. 4, the relative contribution of ttw is small. At 195% deformation, the proportions of activated systems are: 57% for prismatic mode, 35.2% for pyramidal slips $\langle c+a\rangle$, 7.8% for pyr$\langle a\rangle$ and 0% for tensile twinning. Finally, we obtain a reasonable distribution in agreement with the experimental observations: prismatic glide is the main active mechanism, pyramidal slip is a secondary slip mode and twinning contributes very little to the plastic deformation. The weak activation of the tensile twinning is normal because it preferentially reorientates the grains which $\vec{c}$ axes are closed to the RD.

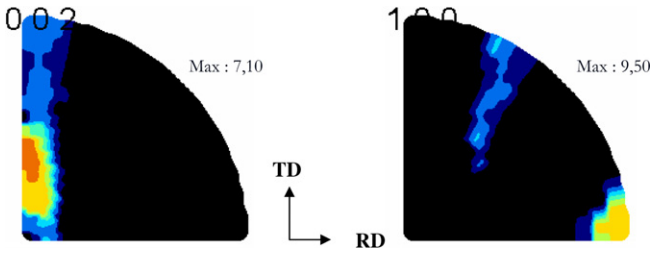

Fig. 3. Predicted PF {0002} and {10$\bar{1}$0} after the cold-rolling process (195% strain).

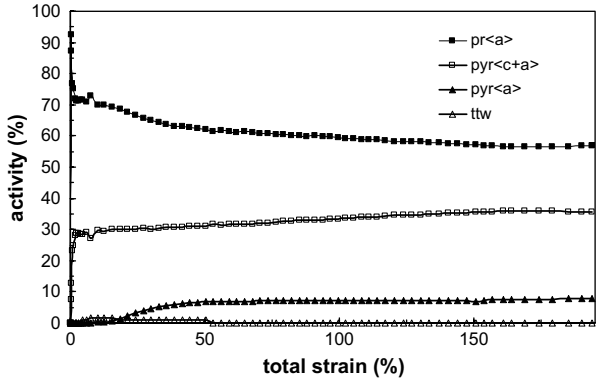

Fig. 4. Relative contribution of each deformation mode to the total shear as a function of deformation.

The theoretical values of the $\langle\varepsilon^{\mathrm{IIth}}(\phi,\psi,hkil)\rangle_{V_d}$ strain were predicted by the EPSC model for 195% strain. Applying Eq. (1) and fitting the results obtained from the model to the experimental data obtained from the six crystallographic planes, the first-order stress tensor element σ_{11}^{I} and the q factor were determined. The results were

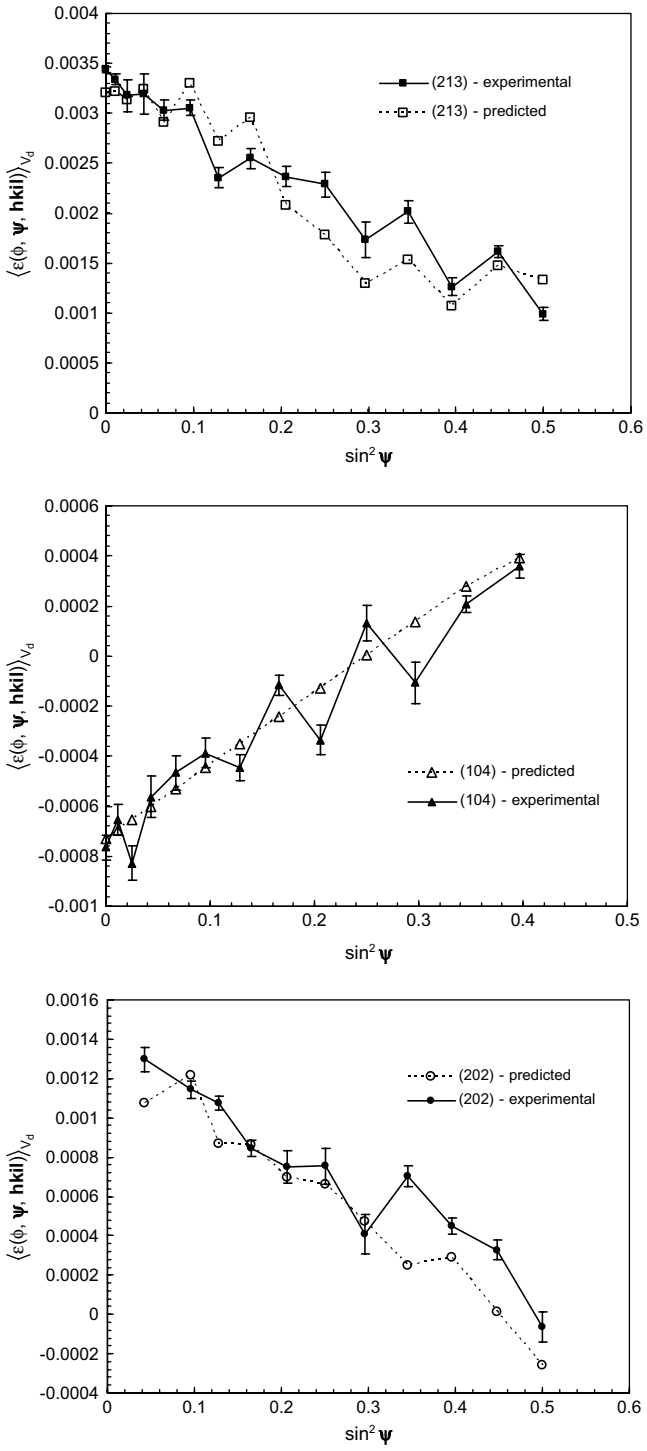

Fig. 5. $\langle\varepsilon(\phi,\psi,hkil)\rangle_{V_d}$ vs. $\sin^2\psi$ estimated using the fitting procedure. The experimental points are shown for 195% strain along the rolling direction.

Table 3
Comparison of the stress values determined by two assumptions, i.e. $\langle \varepsilon^{IIpi}(\phi,\psi,hkil)\rangle_{V_d} \neq 0$ and $\langle \varepsilon^{IIpi}(\phi,\psi,hkil)\rangle_{V_d} = 0$

	q	σ_{11}^{I} (MPa)	
$\langle \varepsilon^{IIpi}(\phi,\psi,hkil)\rangle_{V_d} \neq 0$	0.202 ± 0.081	60 ± 30	
$\langle \varepsilon^{IIpi}(\phi,\psi,hkil)\rangle_{V_d} = 0$	–	$\{10\bar{1}4\}$ plane	$\{21\bar{3}3\}$ plane
		189 ± 16	-334 ± 6

obtained using the $F_{ij}(\phi,\psi,hkil)$ calculated for samples taking into account their texture. In order to visualize the results of the calculation, the $\langle \varepsilon(\phi,\psi,hkil)\rangle_{V_d}$ strain versus $\sin^2\psi$ (evaluated according to Eq. (1)) were compared in Fig. 5 with those measured for the $\{10\bar{1}4\}$, $\{20\bar{2}2\}$ and $\{21\bar{3}3\}$ planes. The predicted results agree with the fact that, in the $\langle \varepsilon(\phi,\psi,hkil)\rangle_{V_d}$ vs. $\sin^2\psi$ representation of the deformed samples, the best fitting for the six studied planes is obtained with prismatic slip as the main deformation mode. In order to show the influence of second-order strain of plastic origin, Table 3 gives the first-order stress calculated with and without the $\langle \varepsilon^{IIpi}(\phi,\psi,hkil)\rangle_{V_d}$ term. σ_{11}^{I} is equal to 60 ± 30 MPa. If the second order 'plastic' stresses are supposed to be null ($\langle \varepsilon(\phi,\psi,hkil)\rangle_{V_d} = F_{ij}(\phi,\psi,hkil)\sigma_{ij}^{exp}(hkil)$), the experimental stresses are then: $\sigma_{11}^{exp}(10\bar{1}4) = +189 \pm 16$ MPa, $\sigma_{11}^{exp}(21\bar{3}3) = -334 \pm 6$ MPa along the RD. This example allows us to conclude clearly that the $\langle \varepsilon^{IIpi}(\phi,\psi,hkil)\rangle_{V_d}$ term plays a key role for a correct interpretation of the X-ray diffraction results. The reliability of q values seems to be correct compared with previous work on cubic material [13]. It can be explained by the overprediction of residual stresses by the self-consistent model. It is a well-known feature of this model [34–36] which is too 'stiff' because it does not take into account the fluctuations of moduli in the matrix and the inclusion due to the nonlinearity of the mechanical behaviour. Elastoplastic properties are considered as uniform inside the crystallites. The formation of a particular microstructure (dislocation band, wall, etc.) inside a crystal is neglected. Discontinuities (grain boundaries, dislocation walls,...) are supposed to have a weak influence on the average behaviour of the aggregate, and dislocations annihilations are not taken into account [37,38]. Nevertheless, the model allows us to describe the evolution of residual stresses whatever the plane. It permits to determine the macroscopic stress. This behaviour can only be explained with prismatic slip as the main deformation mode and for the same set of material parameters. For hexagonal materials alloys, the value of second-order stress is important after large plastic deformation.

6. Conclusions

X-ray diffraction experiments on Zr alloys tubes were used to validate a polycrystal model in the large deformation framework. The present study highlights the usefulness of polycrystal model for exploring the active deformation modes in hcp alloys. Reasonable agreement between model predictions and experimental measurements was observed for both the residual stresses and the evolved deformation textures. Stresses obtained, thanks to X-ray diffraction, are significantly different from one family of lattice planes to another. These results can be explained by the presence of first- and second-order stresses of plastic origin. A self-consistent model has been used to quantify the stress differences between these planes families. The choice of prismatic slip as the main deformation mode can explain *simultaneously* the experimental texture and stress values for the six studied planes. These predicted results can only be obtained for one single set of slip modes and hardening parameters. This analysis shows that X-ray diffraction stress analysis can constitute an effective validation or identification of a model. The influence of second-order strain must be taken into account to get a correct interpretation of X-ray diffraction results for hexagonal material. The method used in this work allows the evaluation of the magnitude of the first- as well as the second-order residual stresses using some additional informations from EPSC model.

References

[1] K. Linga Murty, I. Charit, Prog. Nucl. Energ. 48 (2006) 325.
[2] P. Montmitonnet, R. Logé, M. Hamery, Y. Chastel, J.L. Doudoux, J.L. Aubin, J. Mat. Process. Technol. 125&126 (2002) 814.
[3] E. Girard, R. Guillén, P. Weisbecker, M. François, J. Nucl. Mater. 294 (2001) 330.
[4] D. Gloaguen, M. François, R. Guillén, J. Royer, Acta Mater. 50 (2002) 871.
[5] J.W.L. Pang, T.M. Holden, P.A. Turner, T.E. Masson, Acta Mater. 47 (1999) 373.
[6] P. Zattarin, P. Lipinski, A. Rosochowski, Int. J. Mech. Sci. 46 (2004) 377.
[7] C.N. Tomé, R.A. Lebensohn, U.F. Kocks, Acta Metall. Mater. 11 (1991) 2667.
[8] O. Castelnau, H. Francillette, H. Bacroix, R.A. Lebensohn, J. Nucl. Mater. 297 (2001) 14.
[9] G.C. Kaschner, C.N. Tomé, I.J. Beyerlein, S.C. Vogel, D.W. Brown, R.J. McCabe, Acta Mater. 54 (2006) 2887.
[10] R.A. Lebensohn, M.I. Gonzalez, C.N. Tomé, A.A. Pochettino, J. Nucl. Mater. 229 (1992) 57.
[11] R. Guillén, C. Cossu, T. Jacquot, M. François, B. Bourniquel, J. Appl. Cryst. 32 (1999) 387.
[12] H.R. Wenk, S. Matthies, J. Donavan, D. Chateigner, J. Appl. Cryst. 31 (1998) 262.
[13] A. Baczmanski, K. Wierzbanowski, P. Lipinski, R.B. Helmholdt, G. Ekambaranathan, B. Pathiraj, Philos. Mag A 69 (1994) 437.
[14] H. Dölle, J. Appl. Cryst. 12 (1979) 489.
[15] V. Hauk, Structural and Residual Stress Analysis by Nondestructive Methods, Elsevier, 1997.
[16] I.C. Noyan, J.B. Cohen, Residual Stress – Measurements by Diffraction and Interpretation, Springer-Verlag, 1987.
[17] M. Ortiz, A.A. Pochettino, J. Nucl. Mater. 229 (1996) 65.
[18] B. Dionnet, M. François, J.M. Sprauel, F. Nardou, J. Appl. Cryst. 32 (1999) 883.
[19] E. Kröner, Acta Metall. 9 (1961) 155.
[20] R. Hill, J. Mech. Phys. Solids 13 (1965) 89.
[21] P. Lipinski, M. Berveiller, Int. J. Plasticity 5 (1989) 149.
[22] W. Hutchinson, Proc. Roy. Soc. London A 319 (1970) 247.
[23] P. Zattarin, A. Baczmanski, P. Lipinski, K. Wierzbanowski, Arch. Metall. 45 (2004) 163.

[24] T. Ben Zineb, S. Arbab Chirani, M. Berveiller, in: 15th French Conference of Mechanic, Nancy, France, 2001.
[25] J.P. Lorrain, T. Ben Zineb, F. Abed-Meraim, M. Berveiller, Met. Form. Simul. (2005) 135.
[26] D. Gloaguen, T. Berchi, E. Girard, R. Guillén, Phys. Status Solidi (a) 203 (2006) 12.
[27] A.A. Pochettino, N. Gannio, C. Vial Edwards, R. Penelle, Scripta Metall. 27 (1992) 1859.
[28] E. Tenckhoff, Deformation Mechanisms, Texture, and Anisotropy in Zirconium and Zircaloy, STP 966, 1916 Race Street, PA 19103, Philadelphia, 1988.
[29] A. Akhtar, Acta Metall. 21 (1973) 1.
[30] A. Akhtar, Metall. Trans. 6A (1975) 1105.
[31] A. Akhtar, J. Nucl. Mater. 47 (1973) 79.
[32] G.C. Kaschner, G.T. Gray, Metall. Mater. Trans. A 31 (2000) 1997.
[33] E. Girard, PhD thesis, University of Nantes, France 1993.
[34] R. Masson, M. Bornert, F. Suquet, A. Zaoui, J. Mech. Phys. Solids 48 (2000) 1203.
[35] A. Zaoui, R. Masson, Mater. Sci. Eng. A 285 (2000) 418.
[36] J. Krier, PhD thesis, University of Metz, France 1993.
[37] D. Gloaguen, M. François, Phys. Status Solidi (a) 203 (2006) 1940.
[38] P. Mabelly, P. Hadmar, M. Desvignes, J.M. Sprauel, in: Proceedings of the Fourth European Conference on Residual Stresses, vol. 2, 1996, pp. 941–949.